

Long-wave Infrared Computational Multispectral Metasurface and Spectral Reconstruction Method

SHANG WANG,¹ LIDAN LU,² AND LIANQING ZHU^{3,*}

¹*School of Instrument Science and Opto-Electronics Engineering, Beijing Information Science and Technology University, Beijing, 100192, China*

^{*}*opex@optica.org*

Abstract: We designed a computational multispectral metasurface based on photonic crystals. The study results show that in the 8-11.5 μm wavelength range, the 3 \times 3 photonic crystal array structure exhibits an average transmittance correlation of 0.17, with peak transmittance values ranging from 62.5% to 89.1% and an average energy utilization rate of 32.65% and 49.37%. Additionally, to evaluate the spectral reconstruction performance of the transmission spectra under different photonic crystals, a spectral reconstruction deep learning network was constructed with the mean squared error is 1.292×10^{-3} . This establishes a foundation for future integration on superlattice detectors, aimed at enhancing device integration, reducing system power consumption, and lowering costs.

1. Introduction

Multispectral detection technology integrates the advantages of spatial imaging and spectral detection, utilizing multiple spectral bands to detect and analyze camouflaged objects. This technology effectively distinguishes targets from their backgrounds [1], significantly enhancing detection accuracy and operational effectiveness in military and security environments [2]. Meanwhile, long-wave infrared(LWIR) detection offers strong atmospheric penetration and superior capabilities for identifying camouflaged targets [3]. Superlattice infrared detectors are gaining considerable attention due to their ability to achieve large-format arrays, high spatial resolution, broad spectral response. Therefore, integrating multispectral metasurfaces onto superlattice infrared detector platforms is a promising choice.

Some reports indicate that the majority of computational multispectral metasurfaces for broad-spectrum detection operate in the visible light range, such as quantum dot arrays [4], photonic crystal slab arrays [5], [6], and freeform shaped meta-atoms [7]. In contrast, multispectral filters predominantly employ narrowband filtering metasurfaces [8], [9], which can operate at the cost of time, space, or energy efficiency. Photonic crystals exhibit periodic potentials to incident electrons, and light modulation is achieved by adjusting the constituent materials and geometry of photonic crystals. Micro-spectrometers based on photonic crystals have been integrated on-chip in the visible light range [10], but there are few studies in the LWIR range.

Based on computational spectral demodulation at specific bands, real-time multispectral characteristics can be obtained. Studies have shown that combination of random transmission spectra with spectral information processing algorithms such as least squares [11], CS theory [12], or deep learning [13] can provide highly accurate spectral recognition capabilities. Compared with spectral reconstruction algorithms based on least squares minimization, the main advantage of deep learning methods is the ability to handle large amounts of complex nonlinear data.

In this Letter, we introduce a computational multispectral metasurface based on photonic crystals operating in the LWIR band and a new spectral reconstruction deep learning network. Simulation analyses of photonic crystal parameters. An optimized 3 \times 3 photonic crystal array structure was achieved through design optimization, with higher average energy utilization rates. Meanwhile, using computational algorithms based on deep learning, the spectral information can be accurately reconstructed.

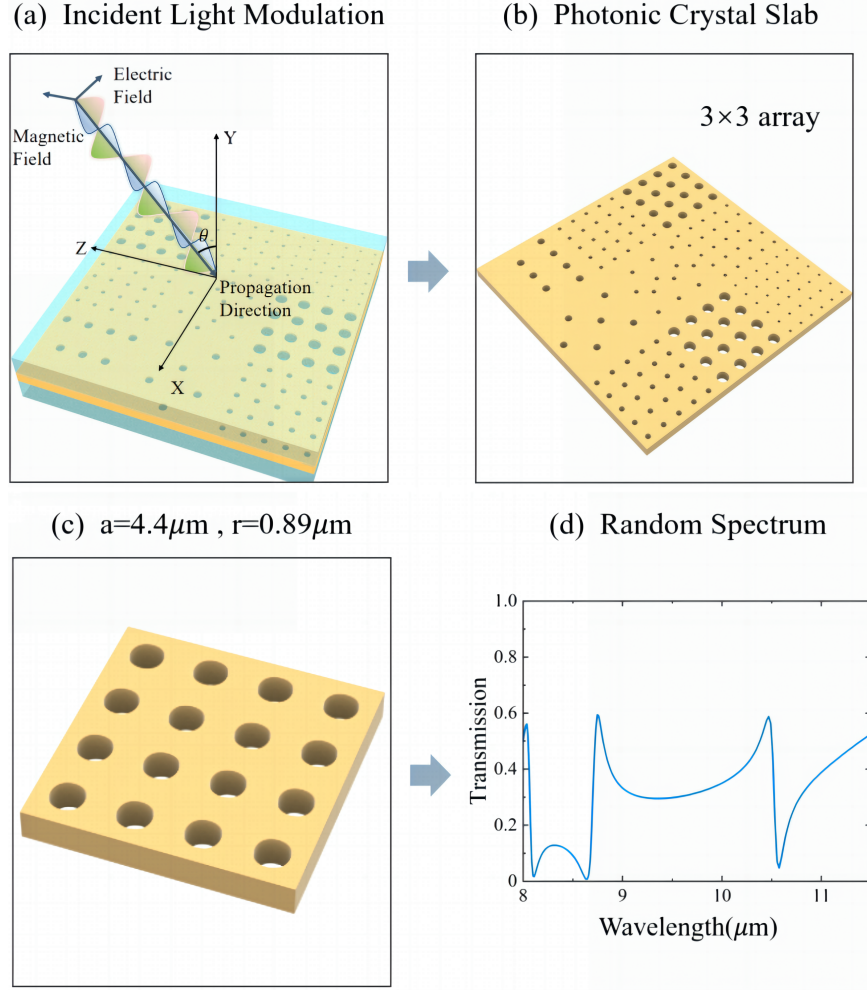


Fig. 1. Schematic diagram of a multispectral metasurface composed of a 3×3 photonic crystal array. (a-b) The 3×3 photonic crystal slab and incident light modulation. (c-d) The photonic crystal array and transmission spectrum.

2. METHODS

Design a schematic of a 3×3 photonic crystal array as shown in Fig. 1. The material selection for the photonic crystal medium substrate emphasizes high transmittance, specifically using GaSb material. As shown in Fig. 1(a,b), during the simulation, the blue parts on the top and bottom layers represent air, while the middle layer consists of a photonic crystal slab made up of a 3×3 array of photonic crystals of varying sizes where the photonic crystal lattice constant ranges from 3.6 to $12 \mu\text{m}$, the hole radius ranges from 0.7 to $2.1 \mu\text{m}$, and the thickness is $1.89 \mu\text{m}$. Rigorous Coupled Wave Analysis (RCWA) is used to simulate the electromagnetic field in the entire three-dimensional structure, obtaining the wavelength response performance influenced by different hole sizes, spacings, and metal thicknesses, and calculating the transmission spectrum of the structure. Incorporate the obtained transmission spectra into the Pearson correlation coefficient calculation to determine the structural parameters with lower correlation coefficients. The photonic crystal array with lattice constant and pore radius of $a = 4.4 \mu\text{m}$, $r = 0.89 \mu\text{m}$ and

its transmission spectrum are shown in Fig. 1(c,d) .

The 3×3 photonic crystal array exhibits nine different transmission spectra in the wavelength range of 8-11.5 μm , as shown in Fig. 2. To calculate the energy utilization rate of the transmission spectrum for different photonic crystal arrays, the total energy within a specific wavelength range can be determined from the spectral data. The results show that the area enclosed by the transmission spectra and the wavelength axis, representing the energy utilization rate, ranges from 21.4% to 47.2%, with an average of 32.7%. The absolute value scatter of the correlation coefficients for photonic crystal arrays is shown in the right panel of Fig. 3. The left panel of Fig. 3 presents a heatmap of the correlation coefficients, with the axes representing different photonic crystal arrays. The mean absolute value of the correlation coefficients between photonic crystal arrays is 0.1697, with the maximum value being 0.3315.

We design an incident spectrum in the wavelength range of 8-11.5 μm composed of multiple random Gaussian functions. The actual spectrum detection simulation also needs to consider experimental noise, which is modeled here as Gaussian white noise. Using a BP (Back Propagation) neural network, the reconstructed spectrum is obtained. This architecture includes

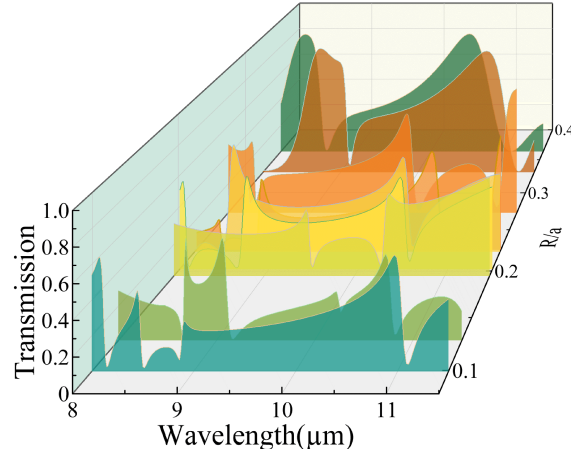


Fig. 2. Transmission spectra of 9 different photonic crystal groups.

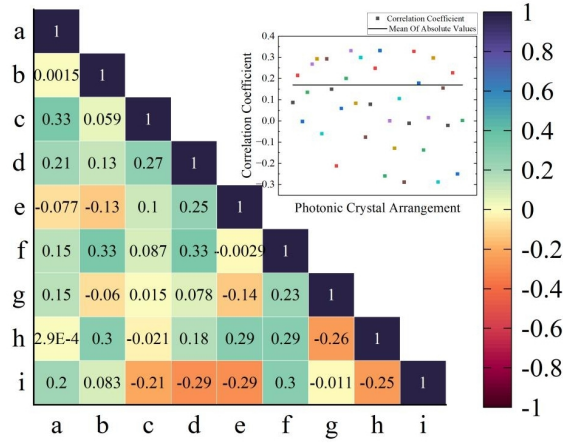


Fig. 3. Pearson Correlation Coefficients between Different Photonic Crystals.

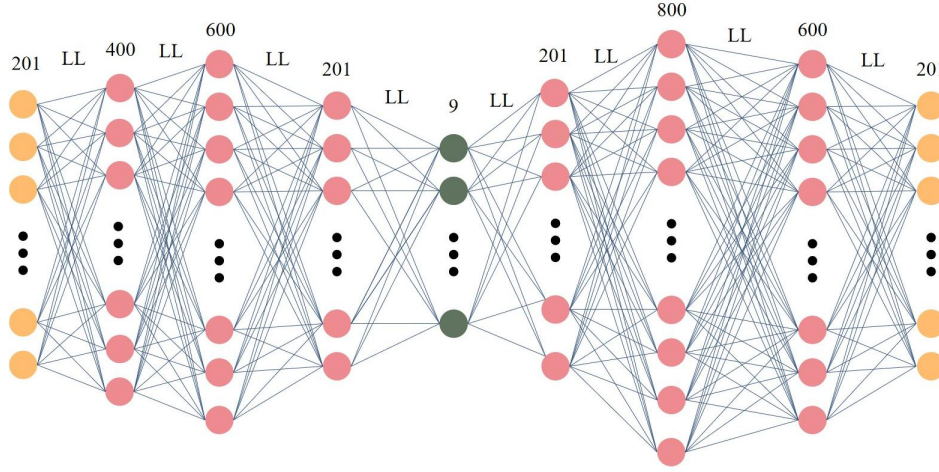


Fig. 4. Schematic Diagram of the Neural Network Architecture for Reconstructed Spectrum Evaluation.

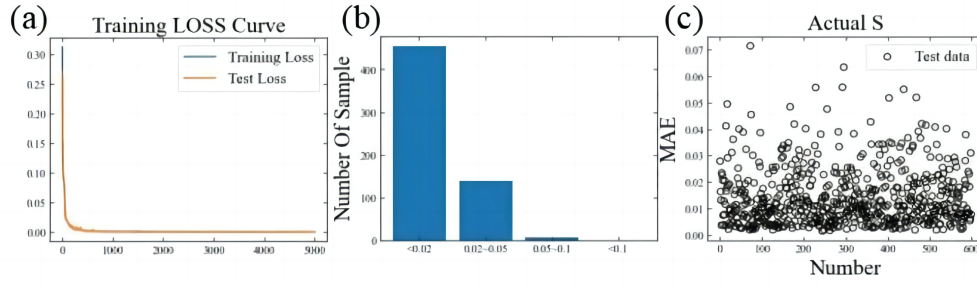


Fig. 5. Deep Learning Results for Photonic Crystal Arrays: (a-c) the loss function curve, the statistical distribution of test set samples within different MAE ranges, and the MAE between the true spectrum and the reconstructed spectrum.

a training and testing dataset of $N = 5000$ incident spectra. In Fig. 6, the BP architecture is as follows: 201-LR-LL-400-LR-LL-600-LL-201-LL-9-LL-200-LR-LL-800-LR-LL-601, where LL represents a linear layer, LR denotes the leaky rectified linear unit. The formula for spectrum reconstruction is as follows:

$$E_i = \int_{\lambda_1}^{\lambda_2} T_i(\lambda) In(\lambda) + n_i d\lambda \approx \sum_{j=1}^N T_i(\lambda_j) In(\lambda_j) + n_i d\lambda. \quad (1)$$

Where $In(\lambda)$ is the incident spectrum, $T_i(\lambda)$ is the transmission matrix, n_i represents experimental noise, and λ_2 to λ_1 ranges from 8 to 11.5 μm , N is the number of points (201), and k is the number of different transmission matrices (9). The loss function is:

$$loss = \min_{In} \|E - TIn\|_2^2 + k \|n_i In\|_2^2. \quad (2)$$

After training and testing cycles, the loss values for the training and testing datasets were reduced to 1.292×10^{-3} and 1.233×10^{-3} , respectively. The statistical distribution of mean absolute error (MAE) and loss function value of the reconstructed spectra and actual spectra of different photonic crystal arrays were calculated. The low loss values indicate that the training

process of Bp performed well in Fig. 7(a). After training, the specific error distribution of the test dataset was analyzed. As shown in Fig. 7(b), it can be seen that most sample data have an MAE error below 0.08, with only 1.4% of the dataset samples having an MAE exceeding 0.05. The mean squared error (MSE) of the test dataset is 1.292×10^{-3} , corresponding to a mean absolute error (MAE = $1/k \sum_{i=1}^k (I_{n_i} - \tilde{I}_i)^2$) of 0.0134 in Fig. 7(c). Among them, \tilde{I}_i represents the reconstructed spectrum. If an MAE < 0.05 indicates high prediction accuracy, then the prediction accuracy of Bp is 98.6%. The results indicate that the MAE statistical distribution is well-formed.

3. Conclusions

A new design with reconstruction algorithm for a multispectral metasurface operating in the long-wave infrared range of 8-11.5 μm has been proposed. Suitable structural parameters were screened based on the correlation coefficient, and the transmission matrix was fed into the reconstruction neural network. The reconstruction errors after training in the region of $[1.292 \times 10^{-3} \sim 1.233 \times 10^{-3}]$, with average energy utilization rates of approximately 32.7% to 49.37%. Deep neural networks, as a data prediction method, significantly improves design efficiency and computational resources. Our results also demonstrate that this design can achieve the purpose of optimizing random multispectral metasurfaces.

References

1. J. S. Silva, I. F. L. Guerra, J. Bioucas-Dias, and T. Gasche, "Landmine detection using multispectral images," *IEEE Sensors J.* **19**, 9341–9351 (2019).
2. N. Takhtkeshha, G. Mandlbürger, F. Remondino, and J. Hyypä, "Multispectral light detection and ranging technology and applications: A review," *Sensors* **24**, 1669 (2024).
3. A. Rogalski and K. Chrzanowski, "Infrared devices and techniques," in *Handbook of optoelectronics*, (CRC Press, 2017), pp. 633–686.
4. J. Bao and M. G. Bawendi, "A colloidal quantum dot spectrometer," *Nature* **523**, 67–70 (2015).
5. Z. Wang, S. Yi, A. Chen, *et al.*, "Single-shot on-chip spectral sensors based on photonic crystal slabs," *Nat. communications* **10**, 1020 (2019).
6. J. Xiong, X. Cai, K. Cui, *et al.*, "Dynamic brain spectrum acquired by a real-time ultraspectral imaging chip with reconfigurable metasurfaces," *Optica* **9**, 461–468 (2022).
7. J. Yang, K. Cui, X. Cai, *et al.*, "Ultraspectral imaging based on metasurfaces with freeform shaped meta-atoms," *Laser & Photonics Rev.* **16**, 2100663 (2022).
8. N. A. Salama, M. Desouky, S. Obayya, and M. A. Swillam, "Free space super focusing using all dielectric hyperbolic metamaterial," *Sci. Reports* **10**, 11529 (2020).
9. R. Chandrasekar, Z. Wang, X. Meng, *et al.*, "Lasing action with gold nanorod hyperbolic metamaterials," *Acs Photonics* **4**, 674–680 (2017).
10. J. Xiong, X. Cai, K. Cui, *et al.*, "Dynamic brain spectrum acquired by a real-time ultraspectral imaging chip with reconfigurable metasurfaces," *Optica* **9**, 461–468 (2022).
11. U. Kurokawa, B. I. Choi, and C.-C. Chang, "Filter-based miniature spectrometers: spectrum reconstruction using adaptive regularization," *IEEE Sensors J.* **11**, 1556–1563 (2010).
12. X. Zhu, L. Bian, H. Fu, *et al.*, "Broadband perovskite quantum dot spectrometer beyond human visual resolution," *Light. Sci. & Appl.* **9**, 73 (2020).
13. C. Brown, A. Goncharov, Z. S. Ballard, *et al.*, "Neural network-based on-chip spectroscopy using a scalable plasmonic encoder," *ACS nano* **15**, 6305–6315 (2021).